Engineering bright fluorescent nitrogen-vacancy (NV) nano-diamonds: Role of low-energy ion-irradiation parameters Ⓕ

Ravi Kumar, Priyanka Pandit, ⒾⒹ **Prabir Pal, et al.**

COLLECTIONS

Ⓕ This paper was selected as Featured

View Online   **Export Citation**   **CrossMark**

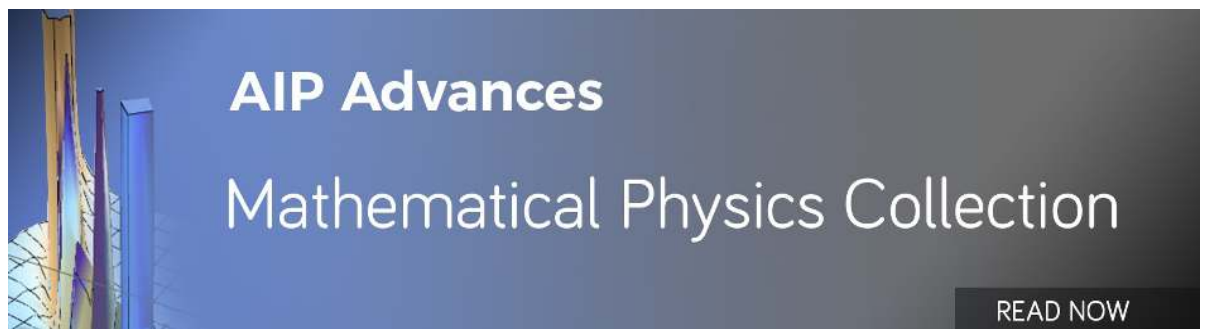## ARTICLES YOU MAY BE INTERESTED IN

Review Article: Synthesis, properties, and applications of fluorescent diamond particles
Journal of Vacuum Science & Technology B **37**, 030802 (2019); https://doi.org/10.1116/1.5089898

Highly intensive emission of the NV^- centers in synthetic HPHT microdiamonds at low nitrogen doping
APL Materials **6**, 086104 (2018); https://doi.org/10.1063/1.5045535

Introduction to quantum optimal control for quantum sensing with nitrogen–vacancy centers in diamond
AVS Quantum Science **2**, 024701 (2020); https://doi.org/10.1116/5.0006785

AIP Advances

Mathematical Physics Collection

READ NOW

Engineering bright fluorescent nitrogen-vacancy (NV) nano-diamonds: Role of low-energy ion-irradiation parameters

Ravi Kumar,[1,2] Priyanka Pandit,[1,3] Prabir Pal,[1,2] S. R. Dhakate,[1,2] R. P. Pant,[1,2] Raj Kumar,[4] Devesh K. Avasthi,[5] and Dilip K. Singh[6,a]

[1]*CSIR-National Physical Laboratory, New Delhi, India, 110012*

[2]*Academy of Scientific and Innovative Research, CSIR-National Physical Laboratory Campus, New Delhi, India, 110012*

[3]*Gautam Buddha University, Greater Noida 201308, U.P, India*

[4]*Inter University Accelerator Centre, Aruna Asaf Ali Marg, New Delhi 110067, India*

[5]*Amity Institute of Nanotechnology, Amity University, Noida 201313, India*

[6]*Department of Physics, Birla Institute of Technology Mesra, Ranchi 835215, India*

Bright emission from fluorescent nanodiamonds (FNDs) is highly desirable for optical bio-imaging applications. Here we report about optimized ion-irradiation and heat treatment conditions for efficient creation of Nitrogen-vacancy (NV) centers in high pressure high temperature (HPHT) grown type Ib Nanodiamond samples irradiated in energy range (20-50 KeV) and at varying fluence (10^{12}-10^{16} ions/cm^2). Different low energy ion irradiations are not detrimental for the crystallinity of nanodiamonds as confirmed by X-ray diffraction and HRTEM. The concentration of defects near the outer surface (non-diamond carbon) has been increased for highest ion dose (50 KeV, 10^{16} ions/cm^2) as compared to lower ion dose (50 KeV, 10^{13} ions/cm^2). The relative emission intensity of characteristic Zero-phonon lines of NV°, NV⁻ centers as compared to broad emission in the range 550-750 nm was monitored with varying NV creation conditions. Sample irradiated at 50 KeV and with fluence of 10^{13} ions/cm^2 show maximum emission in the phonon side band (550-750 nm) with maxima at 680 nm. These optimized ion irradiation conditions leads to the fabrication of 12.5±0.8 ppm concentration of NV⁻ centers in nanodiamonds. This is desirable for their use as biomarker. This work provides a recipe for creating bright nanodiamonds for optical imaging applications. *© 2018 Author(s). All article content, except where otherwise noted, is licensed under a Creative Commons Attribution (CC BY) license (http://creativecommons.org/licenses/by/4.0/).* https://doi.org/10.1063/1.5012068

I. INTRODUCTION

Fluorescent nano particles (FNPs) are highly desirable for optical bio-imaging applications.[1,2] Bio-imaging demands higher photo-stability and bio-compatibility as compared to organic fluorophores and semiconductor quantum dots. The emission of fluorescent marker should be in the range of near infrared (NIR) wavelengths so that it does not overlap with epifluorescence of cells and tissues. Although, semiconductor quantum dots and organic dyes have high quantum yield, but they generally show strong cytotoxicity and poor photo-stability. This limits their use as desirable imaging probe.[3–5] Additionally, the emission from the organic dyes are prone to local biochemical environment.[2,4] Nano diamonds (NDs) incorporated with nitrogen vacancy (NV) color centers shows emission in the range 550-750 nm and are one of the most promising fluorescent markers for optical imaging applications under research.[6] NDs offers two-fold advantage as fluorescent bio marker: (a) They are non-cytotoxic due to chemically inert *sp³*-hybridized carbon structure.[6,7] (b) They can host numerous fluorescent color centers emitting over a wide range of spectra from visible to NIR.[8]

---

[a]Corresponding author. E-mail: dilipsinghnano1@gmail.com (Dilip K. Singh)

Among various carbon nano-materials, NDs shows maximum non-specific cellular uptake into HeLa cell types.[9] Additionally, NDs offers chemically tailorable outer surface[10,11] with presence of oxygen related functional groups (carboxylic, esters, ketonic etc.) enabling it's linkage with different bio molecules in intracellular environment.[12]

NV centers are formed by substitutional nitrogen atom adjacent to a lattice vacancy along <111> direction. NV centers emits in the range 550–750 nm with maxima at ∼ 650 nm (Vibronic side bands in addition to characteristic sharp zero phonon lines (ZPLs) of NV^o (∼ 575 nm) and NV^- (∼ 637 nm). The range of broad emission from NVs (550–750 nm) differs from the fluorescence of different biological chromophores (300-600 nm).[13] The NV^- centers shows very small Debye waller factor (∼ 0.04 %) with typical phonon line width of ∼ 120 nm for phonon side band.[14] In contrast to other fluorescent markers, emission from NV color centers experience limited photo bleaching and blinking.[6,15] The NDs with size < 100 nm has been found to show quantum efficiency approaching 100 %[16] behaving nearly as point source for emission and the refraction effects at diamond air interface become negligible.[17] The concentration of NV centers is much low for as grown NDs (type Ib). But bio-imaging applications require sufficient bright emission from bio markers. Hence multiple NV centers are required per crystallite (∼ 20 nm) for efficient emission collection from NDs. HPHT NDs (type Ib) exhibits fewer structural imperfections and contains very high atomically dispersed substitutional nitrogen (N_s) ∼ 200 ppm. Due to fewer vacancies in as grown HPHT NDs, concentration of NV centers is very feeble. Due to entropy regulations[18] it seems impractical to increase the concentration of lattice vacancies during the growth of diamond in HPHT synthesis.[18]

Ion-irradiation of as grown NDs is usually carried out for fabrication of high density of NV centers. There has been number of attempts using different ions (electron, proton, helium) at wide energy ranges (10 KeV – 10 MeV) to increase the concentration of NV centers.[6,15,19–25] Among different irradiation energy ranges; high energy ion irradiation demands very complex instrumentation due to higher acceleration and focusing mechanism involved. Additionally vacancy creation is highly asymmetric for high energy ion irradiation (Figure 1, supplementary material). Due to large electronic energy losses in their pathways, vacancy creation is limited to the stopping range of ions in the sample. For polycrystalline NDs films with small crystallite size (< 20 nm), maximum sample is left with only electronic energy losses owing to their limited thickness (∼ 0.5 μm). Low energy ion irradiation is suitable alternative for fabrication of NV centers in NDs. For proton and helium ions the threshold incident beam energy is smaller than 1 KeV.[22] Hence protons and helium ions are desirable for fabrication of NV color centers at low energy. He^+ ions are generally preferred over protons due to larger number of vacancies per ion in case of He^+ ion irradiation.[24] Apart from this, the presence of He^+- ions in the diamond lattice does not have any detrimental effect on the emission properties of the fabricated color centers. In addition to lattice vacancy generation through ion irradiation, vacuum annealing plays important role towards NV color center formation. Vacancies migrate at high temperature (≥ 600 °C) and are trapped by substitutional nitrogen atoms (N_s or C-centers) leading to formation of NV centers. He^+-ion irradiation followed by vacuum annealing has been usually carried out for creation of NV centers,[24] but general consensus about optimum beam energy and ion-dose has been lacking in literature.

In this work, we have explored the effect of ion beam energy (20, 30 & 50 KeV) and ion-dose (10^{12}, 10^{13}, 10^{14}, 10^{15} & 10^{16} ions/cm^2) for efficient creation of bright fluorescent NDs. The optimum conditions for creation of nitrogen-vacancy centers in NDs have been established with minimum structural modification to harness maximum emission in the phonon side band: a highly desirable property for their application for bio-imaging applications. Here we report optimum processing conditions for NV center fabrication for optical bio-imaging and two-photon excitation spectroscopy, where large concentration of NV color centers near the surface of NDs is required.

II. EXPERIMENTAL

A. Raw materials and synthesis of NDs

Commercially procured HPHT microdiamonds (element six, MICRON + MDA M0.10) were used as the starting materials for the fabrication of FNDs. Planetary ball milling (250 rpm) of initial

sample (ND0) was carried out for 35 hours (9 hours dry milling, 11 hours wet milling with double distilled (DD) water and subsequent milling with NaCl as the milling media) in the periods of 1 hour milling and 30 minutes break time. Successive breaks in milling prevents the rising of local temperature between milling balls and sample surface and the possibility of the phase change to non-diamond carbon forms was minimized. Milled sample was rinsed with double distilled water to remove NaCl contaminations. Rinsed sample (ND35) was oven dried. Acid reflux of dried sample ND35 was carried out (H_2SO_4: HNO_3 in 3:1 v/v ratio) at 80° C for 8 hours. Sample was repeatedly diluted with double-distilled water and centrifuged (6000 rpm, 5 times). Purified sample (ND35R8) was oven dried (60 °C) and further treated with concentrated HCl at room temperature (4 hours) to etch out the metallic impurities (iron) from the refluxed sample. Sample was repeatedly diluted with water and centrifuged (6000 rpm, 5 times). The finally obtained sample was oven dried. This acid refluxed sample was named as ND35R8HCl. The details of purified sample (ND35R8HCl) have been reported earlier.[26]

B. Sample preparation for ion irradiation of NDs

Acid refluxed NDs (ND35R8HCl) were taken as the target material for ion irradiation. It is due to the fact that acid refluxed NDs are more desirable for optical bio-imaging. Purified NDs were dispersed in double distilled water and drop casted on silicon wafers (100 direction, 1 cm × 1 cm). Samples were oven dried (60° C) for 5 hours. In this way thin films (∼ 0.5 μm) of NDs were prepared on silicon wafers.

C. Fabrication of nitrogen-vacancy (NV) centers

He^+-ion irradiation on NDs was performed using custom made 50 KeV ion accelerator at inter university accelerator center (IUAC), New Delhi. Ion-beam was circular in shape with radius of ∼5 mm and was generated from penning ion source. NDs films were irradiated at three different energies (20, 30, & 50 KeV) at vacuum level of ∼ 5× 10^{-6} torr and at five different ion doses fluences (10^{12}, 10^{13}, 10^{14}, 10^{15}, 10^{16} ions/cm^2). The silicon wafer substrates do not undergo any damage due to limited penetration depth of ions at low energies. Irradiation in the energy range 10 KeV- 45 KeV was carried out using +1 charge state (He^+), while 50 KeV energy irradiation was performed using +2 charge state (He^{2+}) to overcome the acceleration voltage limitation. Irradiated samples were annealed at 750 °C and rotary vacuum level for 2 hours. For the optimization of annealing temperature, samples irradiated at 50 KeV and with ion dose of 10^{13} ions/cm^2 (ND35R8HCl 50 KeV 10^{13}) were annealed in the temperature range 600 – 900 °C.

III. CHARACTERIZATIONS

The particle size and shape were characterized using Transmission electron microscope (TEM) (Model No. FEI Tecnai T30). Raman and Fluorescence spectra of samples were recorded using 514 nm excitation from Ar^+ ion-laser and single monochromator equipped with micro-Raman spectrometer with 50× objective lens using commercial system (Renishaw in Via Raman Microscope) in the backscattering geometry. The concentration of NV centers formed was estimated by comparing the emission intensity (Integrated over the entire spectrum) of different irradiated NDs samples with the known concentration (40 keV, 10^{13} ions/cm^2, 10 ppm).[24] The total emission intensity (integrated peak intensity from 600 nm to 745 nm) of different samples was compared with the reported results (Area under the same region) to calculate the concentration of NV$^-$ centers. The PL was observed at three different points of the samples and the average integrated area was used for comparison. The error in the estimation of concentration of the NV$^-$ centers represents standard deviation in the integrated area for particular sample.

X-ray diffraction pattern (XRD) was recorded using X'Pert Pro PAN analytical X-ray diffractometer at a scanning rate of 0.05 degree/s in 2θ range from 20° to 80° using Cu-K$_\alpha$ radiation (λ=1.54059 Å) in glancing incidence geometry (glancing incidence angle was 1°). The X-ray photoelectron spectroscopy (XPS) measurements were performed by using an Omicron μ-metal ultrahigh vacuum (UHV) system equipped with a monochromatic Al K$_\alpha$ X-ray source (hυ=1486.6 eV) and a multi-channeltron hemispherical electron energy analyzer (EA 125). The samples were mounted on

the sample plates using spot welded Gold foils. An electrical contact was established between the sample surface and Omicron sample plate with a highly conducting UHV compatible Silver (Ag) paint in order to avoid charging during the photoemission measurements due to insulating nature of the samples. The samples were heated *in-situ* at 300 °C under ultra-high vacuum conditions and then cooled down to room temperature before photoemission measurements. This heating procedure helped us to clean the sample surface as confirmed by the absence of surface adsorbed feature around ~532 eV in the O$1s$ core level spectra. The photoemission measurements were performed inside the analysis chamber under a base vacuum of $\sim 5.0 \times 10^{-11}$ mbar at room temperature. The binding energy of all the spectra was calibrated by considering Ag $3d_{5/2}$ at 368.27 eV and the Fermi energy (E_F) from Ag in electrical contact with the sample. The energy resolution was 400 meV in case of XPS spectra using monochromatic Al K$_\alpha$ source. Background intensity arising from secondary electrons from all the core level spectra was subtracted using the Shirley and Tougaard background corrections. EPR spectra was recorded on a X-band reflection type, model E-112 M/s Varian, USA spectrometer.

IV. RESULTS AND DISCUSSION

The goal to maximize NV$^-$ centers per crystallite can be achieved by optimizing the concentration of vacancies. The reported conversion factor from vacancies to NV$^-$ centers is small ($\sim$ 10-23%) due to their annihilation to the surface.[6,23] The desired concentration of vacancies for maximum NV$^-$ creation may also vary depending upon the crystallite size. For type Ib NDs (Ns $\sim$ 100 ppm), the high concentration of vacancies (>100 ppm i.e. > 74 vacancies/crystallite) through the ND crystallites is required. To optimize the vacancy concentration at low energy ion irradiation, the ion dose range from low (10^{12} ions/cm^2) to high ((10^{16} ions/cm^2) for different low energy ranges (10, 20 and 50 KeV) is investigated using Stopping and range of ions in matter (SRIM) software[27] Fig. 1 shows the SRIM calculations (SRIM 2008) for approximate range and concentration of vacancies as He$^+$ ion-beam of different energy irradiates on NDs. In SRIM calculations, [100] (Displacement energy (E_d) of 37.5 eV) has been taken as lattice direction to be damaged.[28] Vacancies and the range would be different for [110] (E_d = 47.6 eV) and [111] (E_d = 45.0 eV) directions.[28] Fig. 1(a) shows the range of ion beams (20, 30 & 50 KeV) in the diamond lattice. 20 KeV ion beam exhibit narrow penetration depth (FWHM $\sim$ 43.7 nm) with maximum damage carried out near 97.7 nm (Average range $\sim$ 93.5 nm). 30 KeV ion beam have slightly larger penetration depth (width $\sim$ 47.7 nm) with maxima at 133.4 nm (Average range $\sim$ 128.4 nm) and exhibits more asymmetry as compared to 20 KeV. 50 KeV ion beam have maximum asymmetry (Width $\sim$ 56.9 nm) in the ion distribution through the ion range with maxima at 194.1 nm (Average range $\sim$ 187.7 nm). The calculated range of ions is only localized to surface for bulk samples but significant for NDs thin films (thickness $\sim$ 0.5 μm).

Fig. 1(b) shows the distribution of lattice vacancies generated by He$^+$ ions of different energies (20, 30 & 50 KeV) in the NDs. Maximum vacancies are formed at the end of ion range. Number of vacancies/ion for different energies is summarized in figure SI (supplementary material). Asymmetry in vacancy creation through the lattice is increased with increase in ion beam energy. Fig. 1(c) shows the electronic and nuclear energy losses for He$^+$-ions in NDs for energy range 10-100 KeV. Electronic energy losses are very feeble at lower ion beam energy. It is due to the fact that lower energy ions have small kinetic energy and longer time to interact with atoms in lattice. Hence lower electronic energy losses and higher nuclear energy losses occurs. With increase of ion energy, the electronic energy loss increases due to increased electronic excitations and associated other phenomenon. Hence, higher energy ions mainly lose their kinetic energy in the forms of electronic energy losses near the surface. It is also clear from figure S1 (supplementary material) where practically no vacancy is formed until ~1 μm of sample thickness. The vacancies are concentrated near the stopping range of ions. It is also clear from figure 1(b) where the asymmetry in vacancy formation increase with ion beam energy.

Fig. 1(d) shows the calculated projected range of He$^+$ ions in NDs for beam energy 10-100 KeV. Target depth of $\sim$ 300 nm could be achieved with ion beams of energy $\sim$ 100 KeV. The nuclear energy losses become insignificant in energy range (50 KeV < E $\leq$100 KeV). Inset of fig. 1(d) shows the
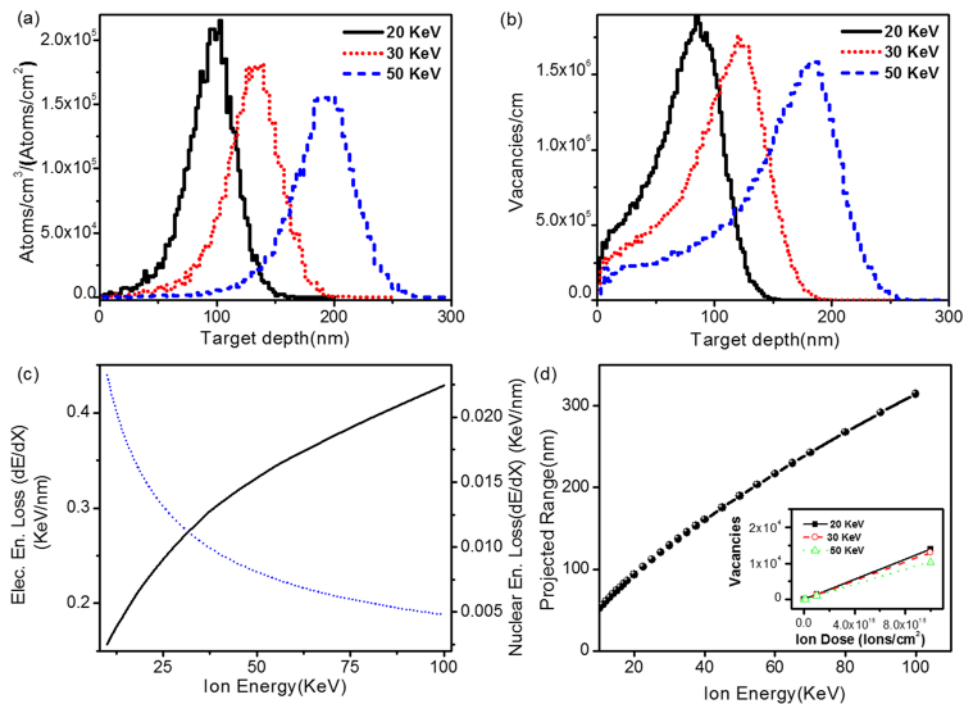
FIG. 1. SRIM calculations for He$^+$ ion beam of different energy (20, 30 & 50 KeV) irradiated on NDs. (a) shows the approximated range for different energy ion beams. (b) Gives the calculation of concentration of vacancies with target depth for different ion beam energy. (c) Shows the SRIM simulations for electronic (black solid curve) and nuclear energy losses (blue dotted curve) for He$^+$ ions in the energy range 10-100 KeV. (d) shows the projected range of He$^+$ ions in energy range 10-100 KeV. Inset of figure (d) gives the approximated number of vacancies for different ion doses (10^{12}-10^{16} ions/cm^2) at three different energies (20, 30 & 50 KeV) of He$^+$ ions.

number of vacancies formed in a 20 nm ND particle by different ion doses (10^{12}-10^{16} ions/cm^2) at three different energies (20, 30 & 50 KeV). It is clear from the figure that relationship between ion-dose and number of vacancies is linear for different energy ion beams. Except the lowest ion dose of all the energies, all the remaining irradiation condition leads to creation of higher vacancy concentration than the concentration of N_s (~100 ppm) as shown in Table III. 20 KeV ion beams creates maximum number of vacancies (steeper slope) among different investigated energies. It is due to narrower region of total nuclear interaction for 20 keV as compared to 30 and 50 keV.

Fig. 2 shows the high resolution transmission electron micrographs of (a) Initial sample ND-0, (b) Milled and purified sample (ND35-R8HCl) and (c) sample irradiated at 50 KeV energy and ion dose of 10^{13} ions/cm^2 (ND35-R8HCl-50KeV-10^{13} dose) and (d) sample irradiated at 50 KeV with a dose of 10^{16} ions/cm^2 (ND35-R8HCl-50KeV-10^{16} dose). The particle size for different NDs is summarized in Table-I. High resolution lattice images of these samples are shown in Fig. 2(e) to Fig. 2(h) respectively. Fig. 2(i)–(l) shows selected area electron diffraction (SAED) pattern for individual ND particles. Inter-planar spacing, particle size and SAED analysis was carried out by using ImageJ software. Assignment of the lattice plane for experimentally observed lattice plane spacing is carried out with reference to PCPDF database #060675. As per PCPDF database #060675 the inter-planar spacing in diamond is observed at 0.206 nm (111), 0.126 nm (220), 0.107 nm (311), 0.089 nm (400) and 0.082 nm (unassigned) respectively. The inter-planar lattice spacing was estimated from SAED pattern by taking average of multiple fringes.

For initial (ND0) and purified samples (ND35R8HCl) inter planar spacing (111) was observed to be 0.210 nm as seen in fig. 2(e) and 2(f). For irradiated sample (50 KeV with 10^{13} ions/cm^2) inter planar spacing from HRTEM was evaluated as 0.185 nm (111) as seen in fig. 2(g). Inter-planar spacing for (111) plane was calculated as 0.213 nm for sample irradiated at energy 50 KeV and fluence of 10^{16} ions/cm^2. As seen in fig. 2(e), the initial sample (ND0) exhibit regular diamond lattice structure with disorderness in lattice structure at the outer layers. This is expected for NDs
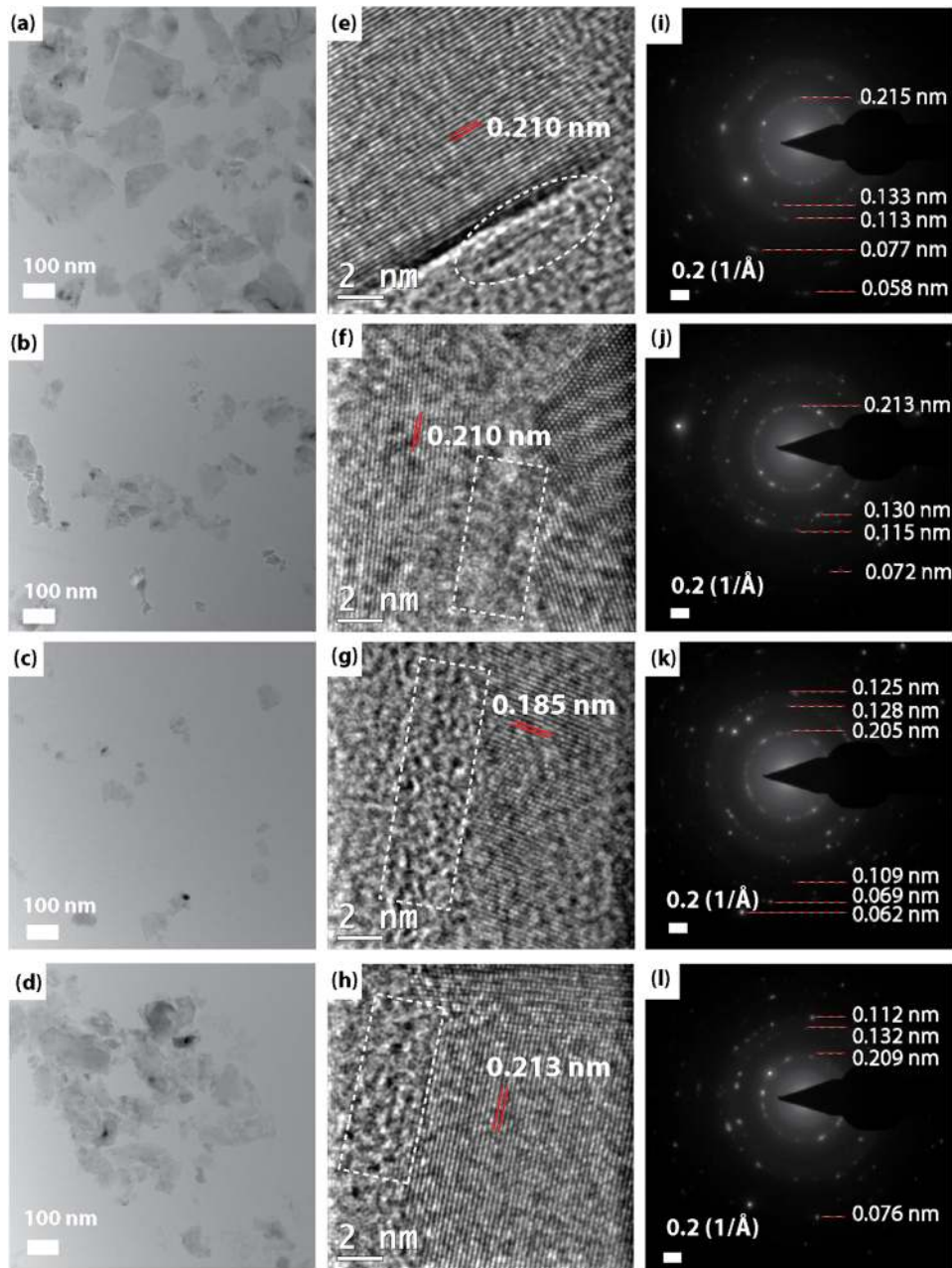
FIG. 2. TEM Image of (a) Initial sample (ND0), (b) Milled and purified sample (ND35R8HCl), (c) Sample irradiated with He$^+$ ions, 50 KeV energy and 10^{13} ions/cm^2 dose (d) sample irradiated with He$^+$ ions of 50 KeV energy and 10^{16} ions/cm^2 dose. Figure (e) to (h) shows the HRTEM images of different samples: (e) ND0, (f) ND35R8HCl, (g) Irradiated with He$^+$ ions of 50 KeV and 10^{13} ions/cm^2 dose, (h) sample irradiated with He$^+$ ions of 50 KeV and 10^{16} ions/cm^2 dose. Interplanar spacing are marked (red) and seen in the micrographs. Figure (i) to (l) shows the SAED pattern analysis carried over individual ND particles with the respective inter-planar spacings. (i) ND0, (j) ND35R8HCl, (k) sample irradiated with He$^+$ ions of 50 KeV energy and 10^{13} ions/cm^2 dose (l) sample irradiated with He$^+$ ions of 50 KeV energy and 10^{16} ions/cm^2 dose. The inter-planar spacing varies from one sample to another due to variation in lattice stress and vacancy concentration.

due to the fact that outer non-diamond cores gives stability to otherwise metastable diamond phase at normal temperature and pressure conditions. Milling and oxidation leads to partial etching of the outer surface but non diamond carbon is still present at outer core as seen from fig. 2(f). It is also clearly seen from the figure that two adjacent ND particles are agglomerated to each other by outer cores of non-diamond carbon. This explains observed agglomerated NDs even after planetary ball

TABLE I. Particle size (HRTEM) and crystallite size (XRD) for initial and irradiated NDs.

Sample	Particle size (nm) (HRTEM)		Crystallite size (nm) (XRD)
	Length	Width	
ND0	203.2 ± 68.8	137.9 ± 56.1	19.7 ± 0.2
ND35R8HCl	102.07 ± 24.6	77.9 ± 43.8	21.8 ± 0.3
ND35R8HCl 50KeV 10^{13}	129.91 ± 61.0	87.5 ± 43.2	21.0 ± 0.1
ND35R8HCl 50KeV 10^{16}	171.4 ± 86.9	110.4 ± 44.8	21.0 ± 0.1

milling.[26] De-agglomeration of NDs up to primary particle level (∼ 20 nm in the present case) requires complete etching of sp^2 carbon. Inter planar spacing (111) for purified NDs irradiated with 50 KeV ion beam at fluence of 10^{13} and 10^{16} ions/cm^2 was calculated as 0.185 and 0.210 nm as shown in fig. 2(g) and 2(h). Ion-irradiation leads to further enhancement of surface defects and non-diamond carbon phases at the outer surface of NDs as seen in fig. 2(g) and 2(h). In contrast to outer surface, the inner-core of irradiated NDs is intact with regular diamond structure. Defects are localized at the surface of NDs even after He$^+$-ion irradiation experiments.

Fig. 2(i)–(l) shows the SAED pattern taken over individual particles for different NDs. Fig. 2(i) shows the SAED pattern for initial NDs (ND0). Sharp diffraction spots are sitting over diffused concentric rings. It shows the presence of the amorphous features in ND0 in addition to diamond structure. This fact is also verified in HRTEM image of ND0 (fig. 2(e)) where diamond core is encircled with the irregular sp^2 hybridized carbon phases. SAED analysis shows the presence of (220) plane (0.133 nm), (311) plane (0.113 nm) and (400) plane (0.077 nm) in addition to (111) plane (0.215 nm). In purified NDs (fig. 2(j)), the d-spacing of respective planes are smaller than ND0. It shows that milling and subsequent acid reflux leads to some compressive strain in NDs. The d-spacing of respective planes have been further decreased in case of sample irradiated at 50 KeV energy at fluence of 10^{13} ions/cm^2 as seen in fig. 2(k). Lowering of the d-spacing of ion irradiated samples shows that compressive strain has been further enhanced. It is due to defects created by He$^+$ ions at regular lattice positions. Vacancies generated during ion irradiation also contribute towards defects of NDs. In contrast to it, sample irradiated at a fluence of 10^{16} ions/cm^2 (Energy 50 KeV) have been observed to have larger d-spacing for respective planes. The d-spacing for this sample approaches to initial sample (ND0). Increased d-spacing points to the fact that defects have been effectively reduced in the diamond lattice. Agglomeration of NDs (as shown in figure 2(d)) play an important role towards increased d-spacing of these ion irradiated NDs. Due to agglomeration of NDs the surface effects are minimized and d-spacing starts to increase.

Fig. 3 shows the XRD pattern for as received NDs (ND0), milled and oxidized NDs (ND35R8HCl) and ion irradiated NDs at ion beam energy 20 KeV (ion dose ∼10^{13} ions/cm^2), 30 KeV (ion dose ∼ 10^{13} ions/cm^2) and 50 KeV (ion dose ∼ 10^{13} and 10^{16} ions/cm^2). Characteristic diffraction peaks has been deconvoluted using Voigt line shape. Estimation of crystallite size of NDs has been carried out by using Scherrer equation. (111) and (220) planes of as received NDs (ND0) are observed at 43.97^o and 75.39^o respectively. Crystallite size for ND0 is estimated to 19.7±0.2 nm. Purification of NDs by acid reflux leads to some suppression of FWHM (0.44 degree) as compared to ND0. The crystallite size is increased (21.8±0.3 nm) but the position of diffraction peaks does not change (43.97^o for (111) plane). Reduced width of diffraction peak reflects the decrease in the lattice strain due to oxidation. He$^+$-ion irradiation at low ion beam energy (20, 30 and 50 KeV) does not affect the crystallinity of NDs as seen from XRD spectra of different ion-irradiated NDs (figure 3). Sample irradiated with ion beam energy of 20 KeV (10^{13} ions/cm^2 dose) and 30 KeV (10^{13} ions/cm^2 dose) exhibits almost same crystallite size (21.0±0.1 nm for 20 KeV and 20.9±0.2 nm for 30 KeV beam energy) with some variation in FWHM (0.45 for 20 KeV and 0.46 for 30 KeV beam energy) of characteristic (111) plane diffraction (Table I). Diffraction peaks of sample irradiated with ion beam energy of 50 KeV (ion dose ∼ 10^{13} ions/cm^2) are observed at 43.49^o ((111) plane) and 75.4^o ((220) plane) with crystallite size of 21.0±0.1 nm. FWHM of (111) diffraction peak (0.45^o) has been slightly increased compared to purified NDs (ND35R8HCl). Since the crystallinity of NDs irradiated at these irradiation conditions remains unchanged indicating the generation of only vacancies upon
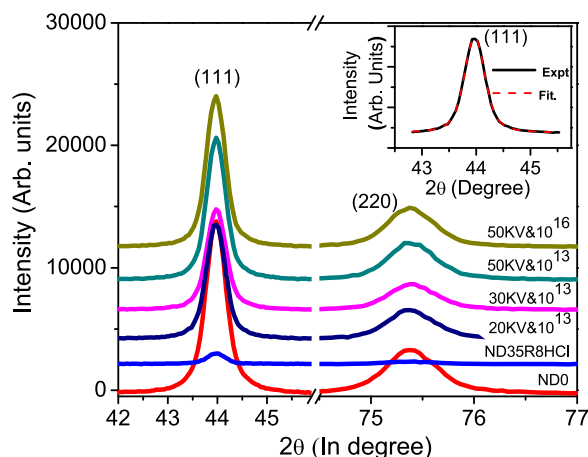
FIG. 3. XRD pattern for as received NDs (ND0), purified NDs (ND35R8HCl) and ion irradiated NDs at different energy and fluence conditions. Despite the surface damage due to He$^+$ ions irradiated NDs shows sharp crystalline features ((111) and (220) planes). Fitted voigt line shape of (111) plane of sample irradiated at beam energy 20 KeV and fluence of 10^{13} ions/cm^2 has been shown in inset.

ion-irradiation. Some disorder may be generated at the outer surface of the crystal, where non diamond carbon phases are already present. As the crystallite size remains same after ion irradiation, generation of amorphous carbon (or graphitic one) pockets within diamond matrix is highly undesirable. This reflects the fact that concentration of vacancies in diamond matrix is much scattered and not localized. This also demonstrate that the average crystal electric field environment should not change significantly in the vicinity of color centers and no anomalous energy level splitting are expected to be observed from fabricated color centers in the fluorescence measurements. Even for the sample irradiated with ion beam energy of 50 KeV (ion dose ~ 10^{16} ions/cm^2) shows diffraction peaks at 43.97º ((111) plane) and ~ 75.3º ((220) plane) with crystallite size of about 21.0±0.1 nm (Table I). Width of (111) diffraction peak (0.45º) is same as for sample irradiated with ion dose of 10^{13} ions/cm^2 (beam energy 50 KeV). Diamond structure does not exhibits structural imperfections and amorphization within the crystalline order of diamond matrix.

Fig. 4 shows the Raman spectra of nano-diamond after irradiation at three different energies (20 KeV, 30 KeV and 50 KeV) in fig (a) to (c) respectively at five doses (10^{12} ions/cm^2, 10^{13} ions/cm^2, 10^{14} ions/cm^2, 10^{15} ions/cm^2 and 10^{16} ions/cm^2). Spectra show two prominent features at ~ 1331 cm^{-1} and at 1580 cm^{-1} referred as D-band and G-band respectively. D-band is related to sp^3-hybridized carbon present in the sample, whereas G-band is related to Graphitic sp^2-hybridized carbon phase. Intensity of the sharp feature at 1331 cm^{-1} decreases with increasing ion-dose, indicating introduction of disorders upon irradiation. With increase of irradiation dose, irradiation introduced disorders nearly suppresses the sharp diamond related feature. In contrast to this, HRTEM studies shows crystalline structure at the core of nanoparticles contains unperturbed diamond like sp^3 crystallinity and damages are localized to surface. This difference in the result arises from limited penetration depth of the laser used for Raman spectroscopy in sp^2 hybridized carbon atoms generated on the outer surface due to irradiation effects.

Fig. 5 shows the XPS spectra of different NDs. Fig. 5(a) shows the survey scan of initial sample (ND0), purified NDs (ND35-R8HCl) and different ion irradiated NDs (20 KeV beam energy at ion-dose of 10^{12} ions/cm^2, 50 KeV ion beam energy at ion-dose of 10^{13} and 10^{16} ions/cm^2 respectively). It is clear from the figure that mainly carbon (core around 284 eV) and oxygen (core around 532 eV) are present in different samples. Except feeble concentration in as received NDs (ND0) nitrogen is absent from all the samples. Nitrogen is not present near the NDs surface for different irradiated NDs. De-agglomeration due to ball milling and presence of oxygen (high electro-negativity) at the outer surface leads to migration of nitrogen towards the center of crystallites. Presence of oxygen was much enhanced after surface functionalization (ND35-R8HCl) as compared to ND0. It shows the attachment of oxygen related functional groups at outer surface and removal of sp^2 carbon species
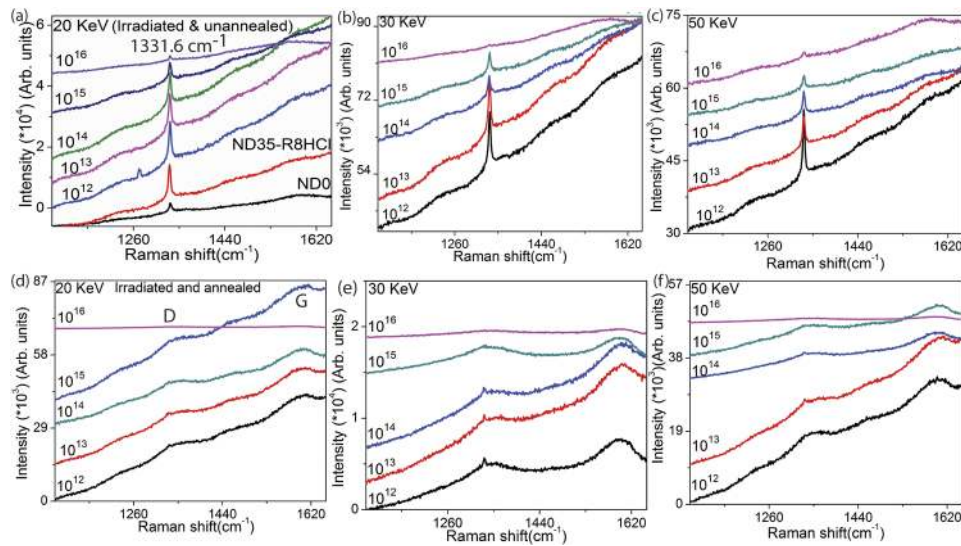
FIG. 4. Raman spectra of He$^+$ ion-irradiated purified nano-diamonds at energy 20 KeV, 30 KeV and 50 KeV and five different irradiation doses (10^{12} ions/cm^2, 10^{13} ions/cm^2, 10^{14} ions/cm^2, 10^{15} ions/cm^2, 10^{16} ions/cm^2). (a) Shows the Raman spectra of sample irradiated at 20 KeV energy and five different ion-doses. (b) and (c) are the unannealed Raman spectra for 30 KeV and 50 KeV beam energy respectively. (d)–(f) shows the Raman spectra of annealed irradiated samples at 20, 30 and 50 KeV energies respectively. Post annealing features of diamond was not clearly visible due to strong fluorescence from created NV centers and surface modification (as evident from intense G band).

effectively. Ion irradiation leads to surface modification and sp^2 carbon species are further enhanced. The oxygen concentration is again reduced for different ion-irradiated NDs as seen from fig. 5(a). Different phases of carbon could not reveal with survey scan.

Fig. 5(b) shows the C$1s$ core spectra for different NDs. C$1s$ core spectra for ND0 is symmetric about the core position (286.5 eV). This reflects the fact that ND0 have negligible fraction of structural defects at the outer surface. Symmetric carbon core reflects the crystalline nature of as received NDs (ND0).[29] Whereas in ND35-R8HCl, C$1s$ core is shifted towards lower binding energy side (~ 285 eV). Surface dangling bonds are terminated with oxygen in different hybridized forms (C-O and C=O). Carbon-oxygen terminated bonds are slightly ionic in nature and binding energy for such bonds is displaced from C$1s$ core towards higher energy side. Ion-irradiation of NDs generates further structural defects at the outer surface and carbon phase is highly disordered within the probe depth (~ 4 nm) of X-rays. This is reflected in the C$1s$ spectra of these NDs (20 KeV & 10^{12} ions/cm^2, 50 KeV & 10^{13} ions/cm^2, 50KeV & 10^{16} ions/cm^2). The C$1s$ core of these irradiated NDs is highly asymmetric toward high binding energy side with a shoulder near the end of C$1s$ core (~ 291 eV).[30] These shoulders are plasmonic losses of π-bonds of graphite phase. Plasmonic losses appear at ~ 6 eV away from C$1s$ core of ion-irradiated samples (Table SIII of the supplementary material). These losses are more prominent in sample irradiated with beam energy of 50 KeV at ion-dose of 10^{16} ions/cm^2 as compared to other samples. As plasmonic losses are characteristics of graphitic phase, ion-irradiation and subsequent annealing leads to phase changes at the outer surface of NDs as observed from Raman spectra. Annealing at 750° C do not improve the crystalline disorders at the outer surface. The plasmon losses for π-bonds in case of as received NDs (ND0) are negligible. It is due to the fact that carbon phases present at the outer surface of ND0 are disordered in nature and the localization of π bonds suppressed the sharp plasmonic features.[30]

Fig. 5(c) shows the fitted C$1s$ core (Gaussian-Lorentzian fitting with Tougard background) for sample irradiated with ion beam energy of 20 KeV at ion dose of 10^{12} ions/cm^2. XPS spectra of other samples were also de-convoluted in similar manner. Fitted peak summary for different NDs samples is given in Table-II. The binding energy positions of different C$1s$ components are listed below. Uncertainty in determining the binding energy position and FWHM is estimated to be ±0.1 eV. Uncertainty in determining peak area and content is estimated to be ±5% of the base value.[31] C$1s$ core spectra of as received NDs (ND0) exhibits sp^2 and sp^3 carbon peaks at 286.2±0.1 eV
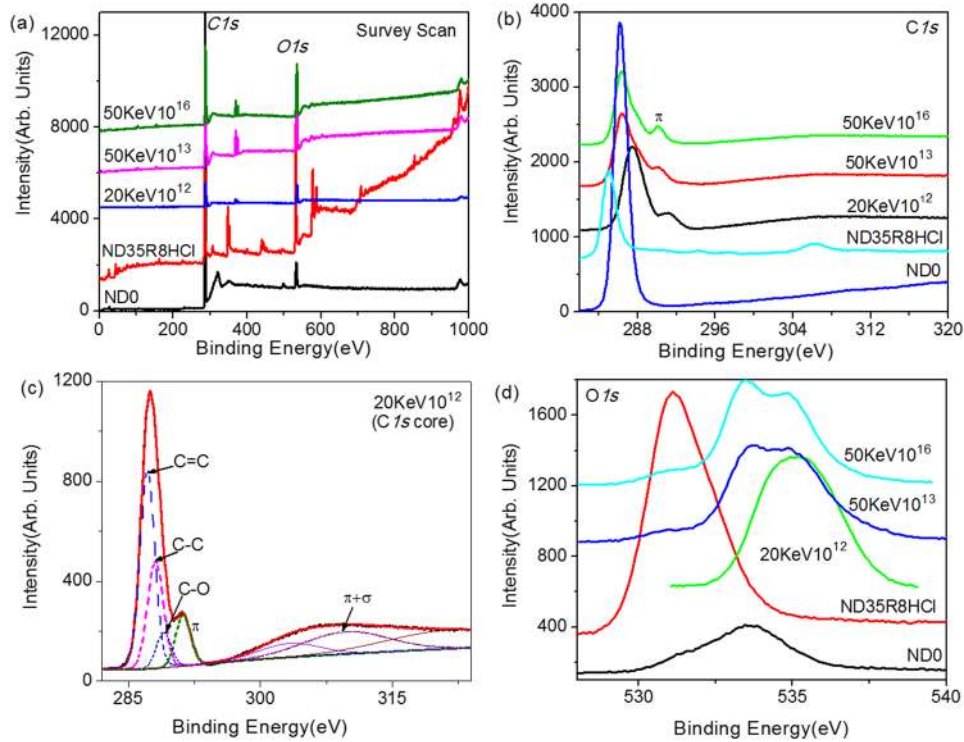
FIG. 5. Shows the XPS spectra for different NDs. (a) shows the survey scan for different NDs. In addition to carbon in different forms, oxygen is also present in NDs. Nitrogen was only observed in initial sample ND0. (b) Shows C*1s* core spectra for different NDs. C*1s* core spectra of different irradiated NDs is shifted from that of ND0. (c) Shows the fitted C*1s* core spectra of ND35-R8HCl-20KeV-10^{12} sample. Presences of high graphitic carbon phase in addition to diamond phase are observed from the figure. (d) Shows O*1s* core spectra for different NDs. Due to purification and oxidation, oxygen core is enhanced and shifted in case of ND35R8HCl sample.

and 286.9±0.1 eV respectively. These peaks are shifted toward high binding energy as compared to reference reported values for sp^2 and sp^3 phases.[32] Shifting of peaks towards higher binding energy is partly due to charging effects in diamond samples. Additionally, the defect at the outer surface also leads to increase in binding energy of C*1s* core.[33] As received NDs are estimated to contain 79.9±4.0 % sp^2 carbon and 20.0±1.0 % sp^3 carbon phases. C*1s* core of de-agglomerated and puri-fied NDs (ND35-R8HCl) is shifted towards lower binding energy. In addition to sp^2 and sp^3 phases, ND35-R8HCl sample also exhibits high concentration of oxygen functional groups (C-O) bonds near the outer surface. The sp^2 and sp^3 carbon phases are downshifted to 285.0±0.1 eV and 286.2±0.1 eV respectively. This sample is estimated to contain 37.4±1.9 % of sp^2 carbon and 24.8±1.2 % of sp^3 car-bon phases. The carbon-oxygen (C-O) bonds are identified at 288.8±0.1 eV with estimated content of 37.8±1.9 %. Apparently the outer surface is highly oxidized and sp^2 carbon phases are drasti-cally reduced as compared to as received NDs. Sample irradiated with ion beam energy of 20 KeV (10^{12} ions/cm^2) shows the upshifting of binding energy of sp^2 (287.2±0.1 eV) and sp^3 (288.1±0.1 eV) carbon phases. This sample is estimated to contain 57.6±2.9 % of sp^2 and 32.4±1.6 eV sp^3 carbon phases. Additionally, carbon-oxygen (C-O) bonding is severely damaged and only 9.9±0.5 wt % content is left (estimated from 289.0±0.1 eV peak). This confirms the outer surface modification upon ion-irradiation. Defect created at outer surface effectively reduces the dangling bonds. Also, 20 KeV ion beam energy has sufficient nuclear energy losses (Fig. 1) to create vacancies in x-ray probe depth (∼ 4 nm). Hence large structural defects are introduced and hybridization of carbon atoms change due to induced heterogeneous local environment in their vicinity near the surface. Local increase in temperature leads to phase change from diamond and amorphous carbon atoms to graphitic phase near the surface. Sample irradiated with ion beam energy of 50 KeV (10^{13} ions/cm^2) exhibits sp^2 (63.8±3.2 wt %) and sp^3 (23.9±1.2 wt %) carbon phases at 286.4±0.1 eV and 288.1±0.1 eV

TABLE II. C*1s* fitted peak parameters for different nanodiamonds. The fitting parameters for the C*1s* core-level spectra shown in Fig. 5(c). The binding energy positions of different C*1s* components are listed below. Uncertainty in determining the binding energy position and FWHM is estimated to be ±0.1 eV. Uncertainty in determining peak area and content is estimated to be ±5% of the base value.

Sample Name	Peak 1	Peak 2	Peak 3	Peak 4	Peak 5	Peak 6	Peak 7	Peak 8
ND0								
Center (eV)	286.2±0.1	286.9±0.1	-	400.1	531.4	533.6		536.3
Area	5673.6±283.7	1419.1±71.0		22.3	116.5	713.2		98.7
FWHM (eV)	1.5±0.1	3.1±0.1		2.3	1.7	2.7		5.0
% content	79.9±4.0	20.0±1.0						
ND35-R8HCL								
Center (eV)	285.0±0.1	286.2±0.1	288.8±0.1		531.0	532.5		
Area	688.3±34.4	456.3±0.1	695.5±34.8	-	2358.7	1270.0	-	-
FWHM (eV)	1.5±0.1	1.8±0.1	6.9±0.1		1.8	1.9		
% content	37.4±1.9	24.8±1.2	37.8±1.9					
ND35-R8HCL 20 KeV 10^{12}								
Center (eV)	287.2±0.1	288.1±0.1	289.0±0.1	-	-	534.2	535.4	535.7
Area	1735.0±86.8	977.8±48.9	300.3±15.0			359.9	1707.8	279.0
FWHM (eV)	2.0±0.1	2.1±0.1	2.0±0.1			1.5	2.7	2.6
% content	57.6±2.9	32.4±1.6	9.9±0.5					
ND35R8HCL 50 KeV 10^{13}								
Center (eV)	286.4±0.1	288.1±0.1	290.2±0.1	-	531.3	533.5	535.0	536.1
Area	1922.1±96.1	720.5±36.0	369.2±18.5		149.5	731.7	848.6	444.1
FWHM (eV)	1.9±0.1	1.8±0.1	1.7±0.1		2.2	1.6	1.9	3.0
%content	63.8±3.2	23.9±1.2	12.2±0.6					
ND35-R8HCL 50 KeV 10^{16}								
Center (eV)	286.3±0.1	287.6±0.1	288.4±0.1	-	531.3	533.3	534.9	-
Area	1693.0±84.6	421.0±21.1	194.9±9.7		129.0	685.8	1330.4	
FWHM (eV)	1.6±0.1	1.5±0.1	1.6±0.1		1.8	1.4	2.1	
% content	73.3±3.7	18.2±0.9	8.4±0.4					
Assignment	*sp²*	*sp³*	*C-O*	*N 1s*		*O1s core*		

respectively. The *sp²* carbon phase is increased in comparison to sample irradiated with ion beam energy of 20 KeV (10^{12} ions/cm²). This is due to increase in ion dose. Due to larger concentration of He⁺ ions the local defect density is increased. But the outermost surface (C-O at 290.2±0.1 eV) is survived more (12.2±0.1 %) as compared to previous irradiated sample. This is due to larger penetration depth and less nuclear energy losses of 50 KeV ion beam in comparison to 20 KeV beam. Sample irradiated with 50 KeV ion beam (10^{16} ions/cm²) exhibits *sp²* (73.3±3.7 wt %) and *sp³* (18.2±0.9 wt %) carbon phases at 286.3±0.1 eV and 287.6±0.1 eV respectively. Hence the outer layers of NDs (up to 4 nm) are highly graphitized. Such high concentration of defects at outer surface is due to very high (10^{16} ions/cm²) concentration of He⁺ ions. Such high concentration of He⁺ ions leads to large vacancy generation per crystallite (∼ 20 nm, Table-SI of the supplementary material). Annealing (at 750° C) leads to migration of vacancies toward the surface of crystallites. At the surface, vacancies are trapped due to presence of defects. Hence the hybridization of surface carbon atoms changes and oxygen is detached from surface carbon. This leads to such high percentage of *sp²* carbon phases at the outer surface. Due to large surface reconstruction, carbon oxygen bonds (288.4±0.1 eV) are reduced up to 8.4±0.4 wt %.

Fig. 5(d) shows the O*1s* core spectra for different NDs. It is clearly seen from the figure that as received NDs (ND0) exhibits very feeble O*1s* core (at ∼534 eV). The purified sample ND35-R8HCl sample on the other hand shows very strong O*1s* core (at ∼532 eV). ND0 shows the weak presence of C=O species (531.4±0.1 eV) like ester and carboxylic groups, nitrosyl (533.6±0.1 eV)

and hydroperoxide (536.3±0.1 eV) groups (Table-II).[34] The presence of C=O (531.0±0.1 eV) and nitrosyl groups (532.5±0.1 eV) are much enhanced in ND35-R8HCl. Functional groups identified with different ion irradiated NDs are also C=O species, nitrosyl and hydro peroxide with varying respective binding energies. This is due to varying local chemical environment near these functional groups at the outer surface of NDs. The positions of O$1s$ core for ion-irradiated NDs are shifted toward higher energy side indicating higher binding energy for both sp^2 and sp^3 hybridized carbon species for these ion-irradiated NDs. Due to structural deformation by ion irradiation, the intensity for different surface functional groups also reduced. Reduction of surface oxygen is also directly results from disturbance of charge neutrality in disordered outer layers. Structural defects causes charge fluctuations at outer surface. These fluctuations reduce the stability of partial ionic bonds between carbon and oxygen or nitrogen.

Fig. (6(a)–(c)) shows fluorescence spectra of purified NDs (ND35R8HCl) irradiated at three different energy (20, 30 and 50 KeV) and at different ion doses (10^{12}–10^{16} ions/cm^2). Figure 6(d) show the comparison of emission intensity for different energy for maximum emission. Ion irradiated NDs shows the characteristic emission of NV color centers. The zero phonon lines (ZPL) of NV^o (~575 nm) and NV$^-$ centers (~637.5 nm) are observed for all irradiated NDs except highest fluence conditions (10^{16} ions/cm^2). Emission from irradiated NDs is extended from 560 nm to 750 nm. Phonon side bands (PSBs) are very prominent and contain most of the emission intensity as reported in literature.[35–37] Width of ZPL varies from one irradiation condition to other (for NV^o centers, FWHM ranges between 4-10.8 nm and in case of NV$^-$ centers ZPL width varies in the range 4-10.2 nm). The broadening of ZPL of NV centers is mainly due to lattice strain. This strain is due to size of NDs and presence of defects due to ion irradiation.[35,38] Irradiation at 50 KeV at dose of 10^{13} ions/cm^2 shows highest fluorescence intensity (Figure 6(d)). Characteristic ZPL emission for
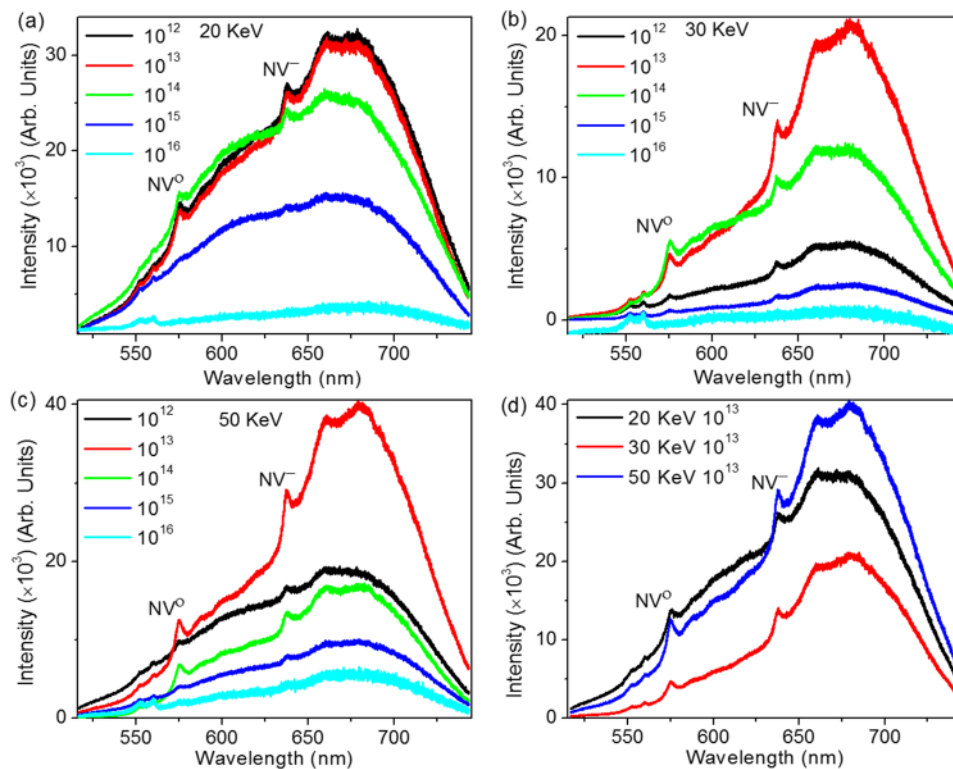

FIG. 6. Shows fluorescence spectra of purified NDs irradiated at three different energy (20 KeV, 30 KeV and 50 KeV) and five dose (10^{12} ions/cm^2, 10^{13} ions/cm^2, 10^{14} ions/cm^2, 10^{15} ions/cm^2, 10^{16} ions/cm^2). Relative emission intensity at different ion doses at irradiation energy of (a) 20 KeV, (b) 30 KeV and (c) 50 KeV. Emission intensity from 10^{16} ions/cm^2 for different energy has been increased by a factor of 9 for comparison. (d) shows the comparison between different irradiation energy for maximum emission. Irradiation at 50 KeV with a dose of 10^{13} ions/cm^2 He$^+$ ions shows highest fluorescence intensity.

NV^o (~575.1 nm, FWHM ~ 4.7 nm) and NV$^-$ centers (~637.9 nm, FWHM ~ 5.2 nm) are sitting over the broad and prominent side bands. The side bands intensity between ZPL of NV^o and NV$^-$ centers is suppressed for the sample irradiated at ion dose of 10^{13} ions/cm^2 (50 KeV). Maximum emission is centered in the side bands of NV$^-$ centers (> 640 nm). It is apparently due to higher concentration of NV$^-$ centers as compared to NV^o centers. Strong side band intensity in near infrared region is due to interaction of lattice phonons with color centers. These interactions are very prominent at room temperature.[39] Highest fluence rate (10^{16} ions/cm^2) for different energies (20, 30 and 50 KeV) results in no resolvable characteristic emission from NV color centers. Broad emission with negligible intensity is present in all the samples irradiated with 10^{16} ions/cm^2 regardless of beam energy. Only the sample irradiated at 50 KeV (10^{16} ions/cm^2) shows weak emission in ZPL of NV^o (~574.7 nm, FWHM ~5.2 nm) and NV$^-$ centers (~637.6 nm, FWHM ~6.9 nm). Absence of color center emission is due to large defects concentration at high fluence. It is also confirmed from HRTEM (Fig. 2) that the outer surface of sample exposed to highest fluence conditions (10^{16} ions/cm^2) shows large concentration of non-diamond carbon. These defects lower the probability of vacancy migration to substitutional nitrogen atoms (N$_s$). High concentration of defects also increases the probability of exciton trapping during the excitation-emission cycle. Trapping of excited electrons in the local defect sites leads to quenching of fluorescence from NV centers.[40,41] Additionally, presence of graphitic outer surface also quenches the fluorescence from NV centers.[42]

Figure 7(a) shows the emission spectra for purified NDs (ND35R8HCl) irradiated with ion beam energy of 40 keV and 50 keV respectively. Ion energy 40 keV and ion dose 10^{13} ions/cm^2 have been reported for the creation of NV centers in NDs. The emission intensity from NV^o centers in 40 keV is higher as compared to that of 50 keV as observed from the spectra (560-620 nm). Whereas, the emission intensity from NV$^-$ centers in 50 keV is much higher as compared to that of 40 keV (620-745 nm). Hence, 50 keV, 10^{13} ions/cm^2 is found to have higher concentration of NV$^-$ centers as compared to 40 keV, 10^{13} ions/cm^2. Further, both of the samples have same spectral features from ensemble emission of NV centers. Figure 7(b) shows the relative emission intensity (integrated over the spectrum) for different irradiated samples. The emission intensity first increases ($\leq 10^{13}$ ions/cm^2) and then decreased abruptly. Maximum emission collection for NV centers (NV^o+NV$^-$) is achieved for 50 keV, 10^{13} ions/cm^2. Sample irradiated with 40 keV, 10^{13} ions/cm^2 have much lower emission collection from NV centers as compared to that of 50 keV, 10^{13} ions/cm^2. The 50 keV, 10^{13} ions/cm^2 have 20% emission contrast as compared to 40 keV. Higher ion dose leads to larger concentration of vacancies but lower NV centers. The lower emission collection from NVs ensemble for higher energy doses is apparently due to conversion of vacancies to lattice defects in spite of their conversion to
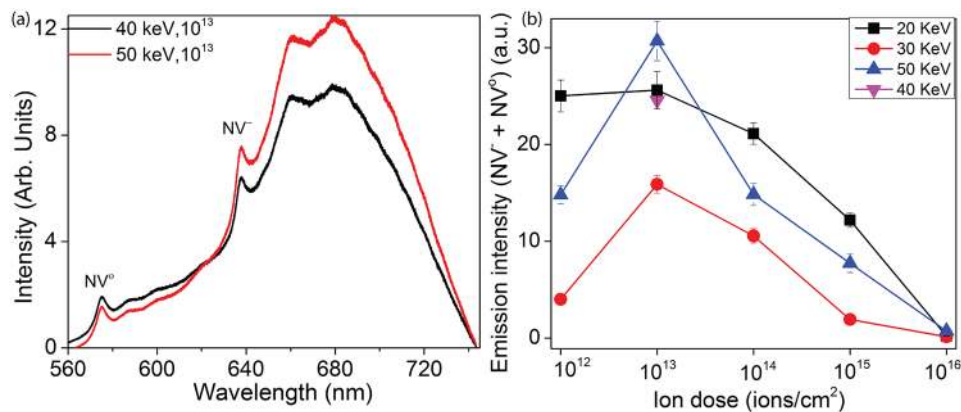

FIG. 7. (a) shows the relative emission from NDs irradiated with 40 keV and 50 keV (10^{13} ions/cm^2). Sample irradiated with 50 keV, 10^{13} ions/cm^2 has much higher emission intensity in PSBs of NV$^-$ centers. (b) shows the relative comparison of emission intensity (integrated over the whole spectrum with linear background) for different irradiated NDs. The maximum emission intensity is associated with 10^{13} ions/cm^2 for different irradiation energy. The emission intensity is highest for 50 keV, 10^{13} ions/cm^2.
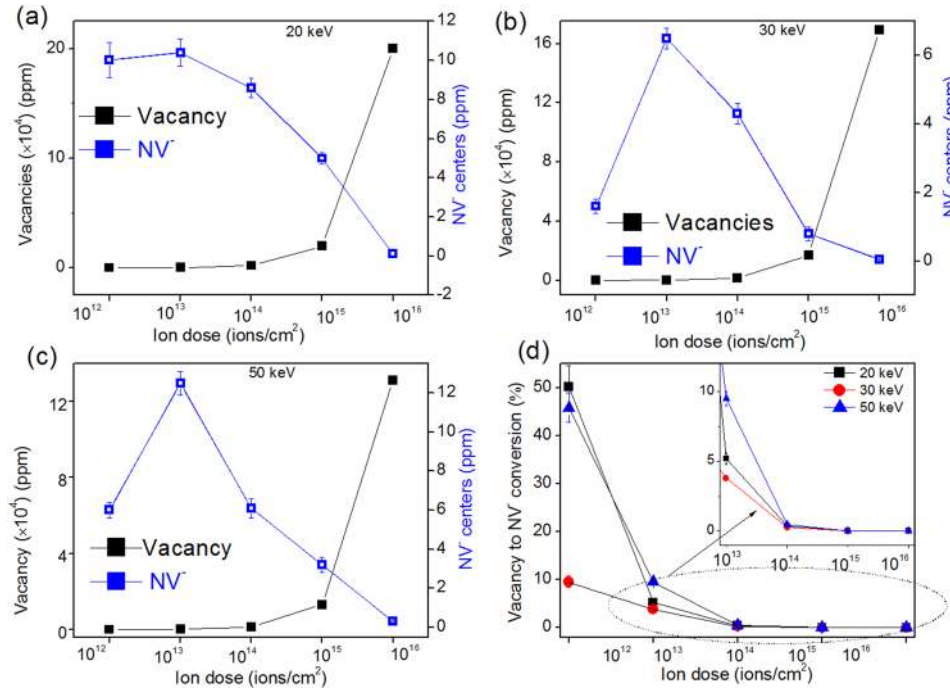
FIG. 8. Shows the concentration of vacancies and NV⁻ centers fabricated (a) for 20 keV (b) for 30 keV and (c) for 50 keV. (d) shows the conversion efficiency for different irradiated NDs from vacancies to NV⁻ centers. The conversion is maximum for minimum ion dose (10^{12} ions/cm^2). As the ion dose increases, the vacancy to NV⁻ conversion drops drastically and becomes minimum for 10^{16} ions/cm^2. Inset of (d) shows the conversion efficiency for ion dose $\geq 10^{13}$ ions/cm^2.

NV centers. This trend is also supported by Raman spectra for irradiated and annealed NDs (Fig. 4 and S3 of the supplementary material).

Figure 8 shows the relative comparison of concentration of vacancies and NV⁻ centers for different irradiated NDs. The NV⁻ centers have been calculated by taking the concentration of NV⁻ centers for 40 keV, 10^{13} ions/cm^2 (10 ppm) as comparison[23,24] The results have been summarized in Table III. Figure 8(a) shows the concentration of vacancies and NV⁻ centers for ion energy of 20 keV. The

TABLE III. Concentration of vacancies and fabricated NV⁻ centers for different irradiated NDs.

Ion energy (keV)	Ion dose (ions/cm2)	Total vacancies	Vacancy concentration (ppm)	NV⁻ concentration (ppm)	Vacancy to NV⁻ conversion (%)
	10^{12}	26×10^{12}	20	10.0±0.9	50.1±4.5
	10^{13}	26×10^{13}	200.2	10.4±0.8	5.2±0.4
20	10^{14}	26×10^{14}	2002	8.6±0.5	0.4±0.02
	10^{15}	26×10^{15}	2.0×10^4	5.0±0.3	0.03±0.002
	10^{16}	26×10^{16}	2.0×10^5	0.1	0.0001
	10^{12}	30×10^{12}	16.9	1.6±0.2	9.5±1.2
	10^{13}	30×10^{13}	169	6.5±0.3	3.8±0.2
30	10^{14}	30×10^{14}	1690	4.3±0.3	0.25±0.02
	10^{15}	30×10^{15}	1.69×10^4	0.6±0.2	0.005±0.001
	10^{16}	30×10^{16}	1.69×10^5	0.05±0.02	0.00003
	10^{12}	34×10^{12}	9.7	6.0±0.4	45.8±3.1
	10^{13}	34×10^{13}	96.6	12.5±0.8	9.5±0.5
50	10^{14}	34×10^{14}	966.1	6.1±0.5	0.5±0.04
	10^{15}	34×10^{15}	9.7×10^3	3.2±0.4	0.02±0.004
	10^{16}	34×10^{16}	9.7×10^4	0.3±0.04	0.0002

concentration of vacancies for 10^{12} ions/cm^2 is 20 ppm. Whereas, the concentration of fabricated NV$^-$ centers is 10.0±0.9 ppm. The concentration of vacancies is directly proportional to ion dose. But the NV$^-$ centers are not created in the same proportion. The maximum concentration of NV$^-$ centers at this energy is 10.4±0.8 ppm (10^{13} ions/cm^2). The concentration of NV$^-$ centers decreases after this ion dose and becomes minimum for 10^{16} ions/cm^2 (0.1 ppm). The concentration of vacancies and NV$^-$ centers follows the same trend for ion energy of 30 keV. The maximum concentration of fabricated NV$^-$ centers at this energy is 6.5±0.3 ppm at ion dose of 10^{13} ions/cm^2. The vacancy to NV$^-$ conversion ratio is much lower for 30 keV. Minimum concentration of NV$^-$ centers was 0.05 ppm (10^{16} ions/cm^2). The maximum concentration of NV$^-$ centers among all the irradiated NDs is 12.5±0.8 ppm (50 keV, 10^{13} ions/cm^2) as shown in figure 8(c). The vacancy and NV$^-$ centers follows the same trend in terms of their concentration as was observed in the previous samples. The maximum conversion of vacancies to NV$^-$ centers is achieved for 20 keV, 10^{12} ions/cm^2 (50.1±4.5%) and closely approached by 50 keV, 10^{12} ions/cm^2 (figure 8(d)). The high conversion efficiency for lowest ion dose is apparently due to the presence of much higher concentration of N_s in the lattice (100 ppm) as compared to fabricated vacancies. This leads to high probability of vacancy to NV^o conversion upon annealing. Further, extra electrons were also supplied by neighboring N_s to provide the extra charge (NV$^-$) to NV centers. In terms of conversion from Ns to NV$^-$, the conversion efficiency comes out to be ~ 10%. It is much lower as compared to estimated conversion efficiency for 100 nm ND crystallite (~20%).[23,43] But as the ion dose increases, the vacancy concentration becomes higher as compared to N_s. This makes the migration and annihilation of vacancies to surface more probable. In addition to this, the defects concentration increases rapidly with increasing ion dose.[44] The local defects may trap the extra electrons from Ns and reduce the concentration of NV$^-$ centers in respective crystallite. The maximum number of NV$^-$ centers per 20 nm crystallite was calculated to be 9.2±0.6 (50 keV, 10^{13} ions/cm^2). These samples were also analyzed using electron spin resonance (ESR) spectroscopy (Fig. S2, supplementary material) to estimate the number of free spins as enlisted in table-SII of the supplementary material. The initial sample contains 1026 spins/gm, while the purified samples contains 873 spins/gm. The samples irradiated at 20 KeV, 30 KeV and 50 KeV (all at 10^{13} dose) and annealed contain 26, 77 and 25 spins/gm. The concentration of free spins associated with substituted nitrogen atoms reduces upon formation of Nitrogen-vacancy (NV) centers. This is in agreement with observed highest fluorescence intensity for sample irradiated at 50 KeV followed by 20 KeV and then 30 KeV as shown in Fig. 6.

Fig. 9(a) shows the PL spectra of samples irradiated at optimized ion dose (50 KeV and 10^{13} ions/cm^2) at different annealing temperature. It is clearly seen from the figure that at temperature ≥ 600 °C, the characteristic emission from NV centers are observed. But at temperature 600 °C,
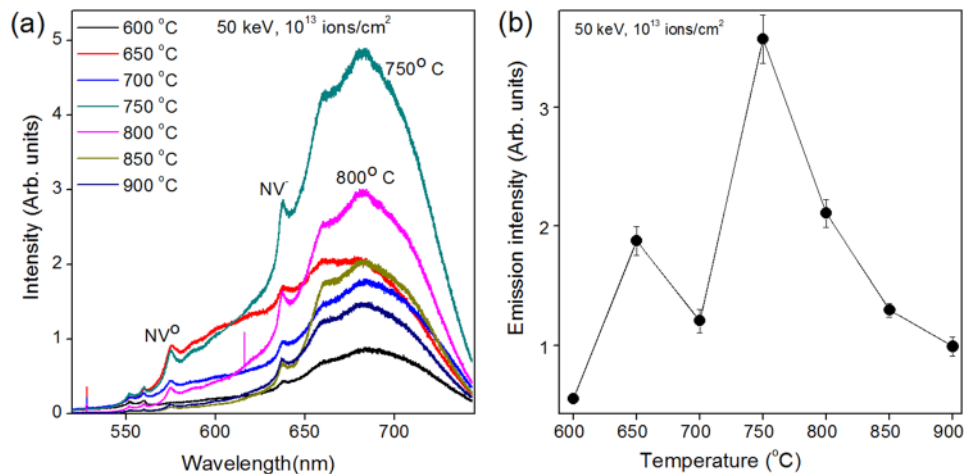

FIG. 9. (a) PL spectra of ion irradiated NDs (ND35R8HCl, 50 KeV, 10^{13} ions/cm^2) at different annealing temperature. Vacuum annealing at 750 °C leads to highest emission intensity in vibronic side band region of NV$^-$ color centers. (b) shows the relative emission collection from different NDs. The emission collection is maximum 750 °C and then reduced drastically.

the intensity of characteristic zero phonon line of NV^o and NV$^-$ centers is very weak. In addition to this, vibronic side bands of NV centers are very weak. It is due to the fact that at 600 ^{o}C all of the available lattice vacancies could not migrate to their energetically favorable positions. Due to their limited migration, substitutional nitrogen atoms could not trap lattice vacancies much. Hence their characteristic emission is much less. At 650° C, the ZPL and vibronic side bands of both NV^o and NV$^-$ are more intense. But, the emission is comparable in NV^o ($\leq$ 620 nm) and NV$^-$ ($\geq$ 620 nm) region. Hence, the concentration of NV^o and NV$^-$ centers is also comparable. Increase in temperature (600 ^{o}C to 650 ^{o}C) causes much more migration of vacancies and their subsequent trapping by N$_s$ atoms. Intensity should be further enhanced at still higher temperature. But there is a small dip in intensity of vibronic side bands at next higher investigated temperature (700 ^{o}C). Emission intensity of NV centers is further enhanced and becomes maximum at 750 ^{o}C. At this temperature, clearly maximum numbers of vacancies are trapped by nearby N$_s$ atoms and concentration of NV centers becomes maximum. At 750° C, the vibronic side band emission between ZPL of NV^o and NV$^-$ is much suppressed and vibronic side band emission of NV$^-$ centers are further enhanced multifold ($\sim$ 2 times as compared to 700 ^{o}C). Hence, the concentration of NV$^-$ centers is much higher as compared to NV^o centers for these annealing conditions. Further increase in the temperature to 800 ^{o}C leads to decrease in emission intensity. The decrease in the emission is partially due to generation of graphitic carbon at higher temperature. The non-diamond carbon reduces the emission collection from NV centers. Also, these surface defects affect the stability of NV$^-$ centers near the surface. Decrease in emission also occurs due to lattice reconstruction near the color centers. This creates some crystal field distortions. Otherwise these defects in ideal crystal field, traps excitons during excitation-emission cycle leading to suppression of emission with increased temperature. Changes in the local lattice environment also affect the ZPL location of NV$^-$ centers, which is blue shifted in this case. These effects are further enhanced with increase in the temperature. At 850° C and 900° C emission intensity of color centers is further suppressed. But there is not much difference observed in the ZPL position of NV centers. With the increase in temperature, there is the decrease in the concentration of NV centers. But the concentration of NV$^-$ centers is always larger than NV^o. This shows the fact that presence of extra electrons near NV centers is always high after a threshold temperature ($\geq$ 750 ^{o} C). Still higher temperature annealing ($\geq$ 1500 ^{o}C) leads to aggregation of nitrogen atoms as they starts migrating in the lattice.[45]

Fig. 9(b) shows the relative emission collection from irradiated NDs under different annealing conditions. Annealing at 600 ^{o}C leads to lower emission collection from NV centers (ZPL+PSBs). As the temperature increases, the emission collection becomes higher. Maximum emission intensity from NV centers is achieved for 750 ^{o}C. At higher annealing temperature, the emission intensity is again starts decreasing. The emission intensity becomes minimum for 900 ^{o}C. Hence the optimized vacuum annealing conditions were found to be 750 ^{o}C (2 hours). The bio imaging applications requires high emission intensity in 550-800 nm range. Hence, these ion irradiation (50 keV, 10^{13} ions/cm^2) and vacuum annealing conditions are most favorable for biological applications of NDs. The concentration of NV$^-$ centers for these optimized fabrication conditions is found to be 12.5$\pm$0.8 ppm. Emission from such high concentration of NV$^-$ centers is comparable to organic fluorophores like rhodamine.[23]

V. CONCLUSIONS

We have optimized the low energy He$^+$ ion irradiation conditions for the efficient creation of NV centers. NV centers have been successfully fabricated for all ion beam energy 20-50 KeV and fluences 10^{12}-10^{15} ions/cm^2 with varying emission intensity of NV$^\circ$ and NV$^-$ centers in addition to broad emission with maxima at $\sim$ 680 nm (NIR region). It is observed that low energy He$^+$-ion irradiation in the range 20-50 KeV has no detrimental effect on the crystallinity of the NDs. Ion-irradiation is found to lead to surface modifications finally resulting into agglomeration of irradiated NDs as observed from HRTEM. Ion-irradiation energy and fluence is found to govern the emission intensity in 550-750 nm. Sample irradiated at 50 KeV with 10^{13} ions/cm^2 have maximum emission intensity with the concentration of NV$^-$ centers of 12.5$\pm$0.8 ppm. The number of NV$^-$ centers per crystallite ($\sim$20 nm) was 9.2$\pm$0.6. Such high concentration of NV- centers in such small crystallites is unprecedented. The

vacancy to NV⁻ conversion for the optimized fabrication conditions was 9.5±0.5%. Sample irradiated at 50 KeV with 10^{13} ions/cm^2 shows suppressed emission from the side bands of NV° centers and maximum emission from side bands of NV⁻ centers (640-750 nm). This emission intensity profile is also supported by much higher emission in ZPL of NV⁻ centers as compared to NV° centers for this sample. Hence irradiation condition of 50 KeV and 10^{13} ions/cm^2 dose is observed to be optimized ion-irradiation condition for the efficient fabrication of NV centers with preferable higher concentration of NV⁻ centers. Post-irradiation, the annealing at 750° C was found to be optimum temperature for formation of NV centers as reflected from maximum fluorescence intensity. At higher temperature ($\geq$750° C), the emission intensity from NV centers reduced drastically. This is due to generation of higher fraction of non-diamond carbon near the surface of ND crystallites. The optimum ion-irradiation conditions established in this work paves way for the synthesis of bright fluorescent NDs by low energy ion irradiation for bio-imaging applications.

SUPPLEMENTARY MATERIAL

See supplementary material for NV centers concentration per ND crystallite as estimated from SRIM). It also includes results and discussion on EPR spectral parameters and calculation of spin concentration. The results of Raman spectra for different samples irradiated at 10^{16} ions/cm^2 at three different energies (20, 30 and 50 KeV) before annealing and post annealing has been included. Details of component of plasmon peak observed in XPS have been tabulated.

ACKNOWLEDGMENTS

[1] M. Bruchez, Jr., M. Moronne, P. Gin, S. Weiss, and A. P. Alivisatos, Science **281**, 2013 (1998).

[2] P. Sharma, S. Brown, G. Walter, S. M. Santra, and B. Moudgil, Adv. Colloid Interface Sci. **123**, 471 (2006).

[3] R. Hardman, Environmental Health Perspect. **114**, 165 (2006).

[4] U. Resch-Genger, M. Grabolle, S. Cavaliere-Jaricot, R. Nitschke, and T. Nann, Nat. Methods **5**, 763 (2008).

[5] S. J. Rosenthal, J. C. Chang, O. Kovtun, J. R. McBride, and I. D. Tomlinson, Chem. Bio. **18**, 10 (2011).

[6] S. Yu, M. Kang, H. Chang, K. Chen, and Y. Yu, J. Am. Chem. Soc. **127**, 17604 (2005).

[7] A. M. Schrand, H. Huang, C. Carlson, J. J. Schlager, E. O. sawa, S. M. Hussain *et al.*, J. Phys. Chem. B **111**, 2 (2007).

[8] I. Aharonovich, S. Castelletto, D. A. Simpson, C. Su, A. D. Greentree, and S. Prawer, Rep. Prog. Phys. **74**, 076501 (2011).

[9] X. Zhang, W. Hu, J. Li, L. Tao, and Y. Wei, Toxicol. Res. **1**, 62 (2012).

[10] Y. Liu, Z. Gu, J. L. Margrave, and V. N. Khabashesku, Chem. Mater. **16**, 3924 (2004).

[11] Y. Liang, M. Ozawa, and A. Krueger, ACS Nano **3**, 2288 (2009).

[12] V. N. Mochalin, O. Shenderova, D. Ho, and Y. Gogotsi, Nat. Nanotechnol. **7**, 11 (2012).

[13] V. Vaijayanthimala and H. C. Chang, Nanomedicine **4**, 47 (2009).

[14] J. E. Field, *The Properties of Natural and Synthetic Diamond* (Academic Press, London, 1992).

[15] A. Gruber, A. Drabenstedt, C. Tietz, L. Fleury, J. Wrachtrup, and C. V. Borczyskowski, Science **276**, 2012 (1997).

[16] G. Davies, *Properties and Growth of Diamond*, EMIS Data Review Series No. 9 (INSPEC, The Institution of Electrical Engineers, London, 1994).

[17] A. D. Greentree, I. Aharonovich, S. Castelletto, M. W. Doherty, L. P. McGuinness, and D. A. Simpson, Opt. Photonics News **21**, 20 (2010).

[18] C. Kittel, *Introduction to solid state*, John Wiley & Sons (1966).

[19] G. Davies and M. F. Hamer, Proc. R. Soc. Lond. A **348**, 285 (1976).

[20] A. Beveratos, S. Kühn, R. Brouri, T. Gacoin, J. P. Poizat, and P. Grangier, Eur. Phys. J. D **18**, 191 (2002).

[21] F. Neugart, A. Zappe, F. Jelezko, C. Tietz, J. P. Boudou, A. Krueger *et al.*, Nano Lett. **7**, 3588 (2007).

[22] C. Fu, H. Lee, K. Chen, T. Lim, H. Wu, P. Lin, P. K. Wei, P. H. Tsao, H. C. Chang, and W. Fann, Proc. Natl. Acad. Sci. U.S.A **104**, 727 (2007).

[23] T. Wee, Y. Tzeng, C. Han, H. Chang, W. Fann, J. Hsu *et al.*, J. Phys. Chem. A **111**, 9379 (2007).

[24] Y. Chang, H. Lee, K. Chen, C. Chang, D. Tsai, C. Fu, T. S. Lim, Y. K. Tzeng, C. Y. Fang, C. C. Han, H. C. Chang, and W. Fann, Nat. Nanotechnol. **3**, 284 (2008).

[25] N. Mohan, C. Chen, H. H. Y. Wu, and H. Chang, Nano Lett. **10**, 3692 (2010).

[26] R. Kumar, S. J. Yoon, K. G. Lee, P. Pal, R. P. Pant, C. K. Suman, S. R. Dhakate, R. Kumar, D. K. Avasthi, and D. K. Singh, RSC Adv. **6**, 47164 (2016).

[27] J. F. Ziegler, J. P. Biersack, and U. Littmark (Pergamon, New York, 1985).

[28] J. Koike, D. M. Parkin, and T. E. Mitchell, Appl. Phys. Lett. **60**, 1450 (1992).

[29] Y. Fan, A. G. Fitzgerald, P. John, C. E. Troupe, and J. I. B. Wilson, Surf. Interface Anal. **34**, 703 (2002).

[30] J. Díaz, G. Paolicelli, S. Ferrer, and F. Comin, Physical Review B **54**, 8064 (1996).

[31] M. J. Webb, P. Palmgren, P. Pal, O. Karis, and H. Grennberg, Carbon **49**, 3242 (2011).

[32] S. T. Jackson and R. G. Nuzzo, Appl. Surf. Sci. **90**, 195 (1995).

[33] I. Kusunoki, M. Sakai, Y. Igari, S. Ishidzuka, T. Takami, T. Takaoka, M. Nishitani-Gamo, and T. Ando, Surface Science **492**, 315 (2001).

[34] G. Cunningham, A. M. Panich, A. I. Shames, I. Petrov, and O. Shenderova, Diamond Relat. Mater. **17**, 650 (2008).

[35] J.-P. Boudou, P. A. Curmi, F. Jelezko, J. Wrachtrup, P. Aubert, M. Sennour, G. Balasubramanian, R. Reuter, A. Thorel, and E. Gaffet, Nanotechnology **20**, 235602 (2009).

[36] J. Wolters, A. W. Schell, G. Kewes, N. Nüsse, M. Schoengen, H. Döscher, T. Hannappel, B. Löchel, M. Barth, and O. Benson, Applied Physics Letters **97**, 141108 (2010).

[37] N. B. Manson, J. P. Harrison, and M. J. Sellars, Physical Review B **74**, 104303 (2006).

[38] F. Jelezko, C. Tietz, A. Gruber, I. Popa, A. Nizovtsev, S. Kilin, and J. Wrachtrup, Single Molecules **2**, 255 (2001).

[39] C. Santori, P. E. Barclay, K.-M. C. Fu, R. G. Beausolei, S. Spillane, and M. Fisch, Nanotechnology **21**, 274008 (2010).

[40] B. R. Smith, D. W. Inglis, B. Sandnes, J. R. Rabeau, A. V. Zvyagin, D. Gruber, C. J. Noble, R. Vogel, E. Ōsawa, and T. Plakhotnik, Small **5**, 1649 (2009).

[41] J. R. Rabeau, A. Stacey, A. Rabeau, S. Prawer, F. Jelezko, I. Mirza, and J. Wrachtrup, Nano Lett. **7**, 3433 (2007).

[42] B. R. Smith, D. Gruber, and T. Plakhotnik, Diamond Relat. Mater. **19**, 314 (2010).

[43] L. Su, C. Fang, Y. Chang, K. Chen, Y. Yu, J. Hsu, and H. Chang, Nanotechnology **24**(31), 315702 (2013).

[44] F. C. Waldermann, P. Olivero, J. Nunn, K. Surmacz, Z. Y. Wang, D. Jaksch, R. A. Taylor, I. A. Walmsley, M. Draganski, P. Reichart, A. D. Greentree, D. N. Jamieson, and S. Prawer, Diamond Relat. Mater. **16**, 1887 (2007).

[45] A. T. Collins, Journal of Physics C: Solid State Physics **11**, L417 (1978).